SCIENTIFIC REPORTS

OPEN

CONFERENCE PROCEEDINGS

APEnergy2014

SUBJECT AREAS:

SYNTHESIS AND PROCESSING

BATTERIES

Received
10 February 2014

Accepted
6 May 2014

Published
29 August 2014

Correspondence and requests for materials should be addressed to Y.C.K. (yckang@konkuk.ac.kr)

One-pot synthesis of manganese oxide-carbon composite microspheres with three dimensional channels for Li-ion batteries

You Na Ko[1,2], Seung Bin Park[2], Seung Ho Choi[1] & Yun Chan Kang[1]

[1]Department of Chemical Engineering, Konkuk University, 1 Hwayang-dong, Gwangjin-gu, Seoul 143-701, Korea, [2]Department of Chemical and Biomolecular Engineering, Korea Advanced Institute of Science and Technology, 291 Daehak-ro, Yuseong-gu, Daejeon 305-701, Korea.

The fabrication of manganese oxide-carbon composite microspheres with open nanochannels and their electrochemical performance as anode materials for lithium ion batteries are investigated. Amorphous-like Mn_3O_4 nanoparticles embedded in a carbon matrix with three-dimensional channels are fabricated by one-pot spray pyrolysis. The electrochemical properties of the Mn_3O_4 nanopowders are also compared with those of the Mn_3O_4-C composite microspheres possessing macropores resembling ant-cave networks. The discharge capacity of the Mn_3O_4-C composite microspheres at a current density of 500 mA g^{-1} is 622 mA h g^{-1} after 700 cycles. However, the discharge capacity of the Mn_3O_4 nanopowders is as low as 219 mA h g^{-1} after 100 cycles. The Mn_3O_4-C composite microspheres with structural advantages and high electrical conductivity have higher initial discharge and charge capacities and better cycling and rate performances compared to those of the Mn_3O_4 nanopowders.

Because of the increasing demand for Li-ion batteries (LIBs) with high power, there is a need for new electrode materials with high performance capabilities. Recently, various transition metal oxides such as MnO_x, CoO_x, NiO_x, and FeO_x have been considered as promising anode materials for LIBs because of their high lithium storage capacity, low cost, and low toxicity[1–5]. However, large volume change of the transition metal oxides during the Li-ion insertion/extraction process, which leads to electrode pulverization and rapid capacity fade, produce limitations for practical applications as anode materials[6–8]. Many methods have been undertaken to overcome the problems of transition metal oxides by modification or fabrication with controlled morphology[9–12].

Among the various techniques, fabrication of composite electrode materials with diverse carbonaceous materials and metal oxides has been demonstrated as a promising strategy for enhancing the electrochemical performance[13–17]. In particular, nano-sized metal oxides embedded in amorphous carbon matrix have been reported to exhibit good cycling stability because amorphous carbon matrix can buffer the volume change and prevent agglomeration of metal oxide during cycling[18–21]. However, the formation of metal oxide-carbon composite materials with large sizes and dense structures increased the lithium ion diffusion path, despite the improvements in electrical conductivity of composite materials[22].

Development of novel metal oxide-carbon composite electrode materials has attracted much attention for enhancing the cycling as well as the rate performance. Fabrication of porous structured metal oxide has been demonstrated as an efficient strategy as the pores can accommodate the strains of Li-ion insertion/extraction and offer a short path for Li-ion and electron transport[23–25]. In particular, porous structured metal oxides with connective and open channels such as the three-dimensional ordered macroporous structure and ant-cave structure have exhibited superior electrochemical performance owing to the connective and open channels permitting electrolyte penetration and fast kinetics[26–30].

Fabrication of manganese oxides with diverse stoichiometric compositions such as MnO, MnO_2, Mn_2O_3, and Mn_3O_4 and application for LIBs has been widely reported because of their abundance and non-toxicity; however, because of their inherent limitations such as poor rate performance and cycling stability, the development of novel structured MnO_x still remains as a great challenge for enhancing electrochemical performances[31–36]. The fab-

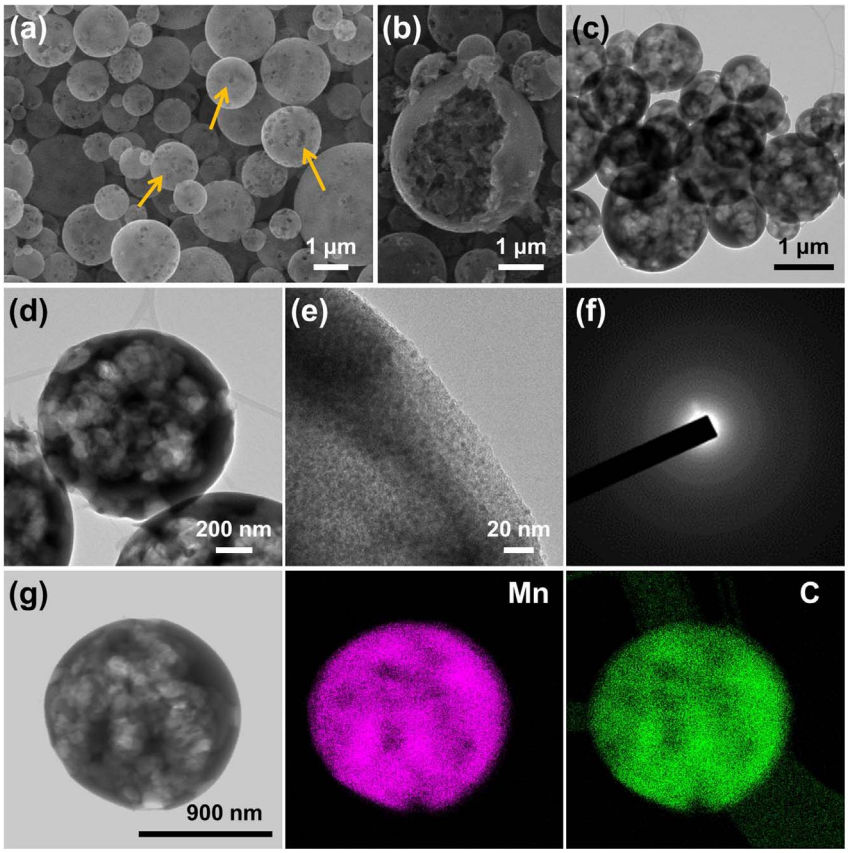

Figure 1 | Morphologies of the Mn_3O_4-C composite microspheres with open-nanochannels: (a) SEM image, (b) SEM image of the crushed powders, (c)–(e) TEM images, (f) SAED pattern, and (g) dot-mapping images.

rication of MnO_x-carbon composite materials with connective and open channels has been rarely reported, though diverse structured MnO_x-carbon composite materials have been extensively investigated.

In this study, we report the fabrication of manganese oxide-carbon composite microspheres with open nanochannels and their electrochemical performances as anode materials for LIBs. Amorphous-like Mn_3O_4 nanoparticles were uniformly embedded in carbon matrix with three dimensional channels. The carbon matrix and open nanochannels are valuable in the accommodation of volume change and facilitation of fast ion transport. The manganese oxide-carbon composite microspheres with three-dimensional channels exhibited superior electrochemical performance compared with those composed of well-faceted nanoparticles with a high degree of crystallinity.

Results

Spherical shape Mn_3O_4-C composites with macropores were prepared by a simple one-pot spray pyrolysis process. The macropores, which are connected within the composite powder producing a system similar to ant-cave networks, can be occupied by liquid electrolytes during cycling to improve the rate performance of the composite microspheres by decreasing Li-ion diffusion distance for Li-ion transfer from or to liquid electrolyte. The carbon component improves the electrochemical properties of the Mn_3O_4-C composite by increasing the electrical conductivity of the powders and minimizing the crystal growth of Mn_3O_4 during the preparation process. The uniform embedding of the Mn_3O_4 nanocrystals in the carbon matrix improves the structural stability of the Mn_3O_4-C composite powders during cycling. The macropores and carbon components also improve the cycling performance of the composite microspheres by acting as buffer layers, which can accept the large volume change of Mn_3O_4 during cycling. In this study, polystyrene (PS) nanobeads, which can be easily decomposed into water vapor and CO_2 gas under nitrogen atmosphere, were applied to form the macropores within the composite powder. The voids formed by decomposition of PS nanobeads resulted in the macropores within the Mn_3O_4-C composite microspheres by structural change at a high preparation temperature of 800°C.

The morphologies of the Mn_3O_4-C composite microspheres prepared directly by spray pyrolysis are shown in Figure 1. The SEM images as shown in Figures 1a and 1b display a spherical shape and macroporous structure. The composite microspheres have nanosized holes non-uniformly distributed over the surface as shown by arrows in Figure 1a. The low resolution TEM images as shown in Figures 1c and 1d also display the macropores within the composite microspheres. The high resolution TEM image as exhibited in Figure 1e reveals the uniformly distributed Mn_3O_4 nanoclusters of a few nanometers in size in the carbon matrix. The selected area electron diffraction (SAED) and XRD pattern as shown in Figures 1f and 2 indicate the amorphous like structure of the Mn_3O_4-C composite microspheres. The XRD pattern of the powders has broad and low intensity peaks arising from the Mn_3O_4 crystals. The amorphous-like Mn_3O_4-C composite microspheres were prepared at a high temperature of 800°C as the carbon matrix disturbs the crystal growth of the manganese oxide. The dot-mapping images as shown in Figure 1g display the uniform distributions of manganese and carbon components in the powder. Phase separation of manganese and carbon components did not occur during droplet drying, decomposition of manganese salt, and carbonization of sucrose. The carbon content of the Mn_3O_4-C composite microspheres measured by thermogravimetric (TG) analysis as shown in Figure S1 is 49 wt%.

The Mn_3O_4 nanopowders were also prepared for comparison of their electrochemical properties with those of the Mn_3O_4-C compos-

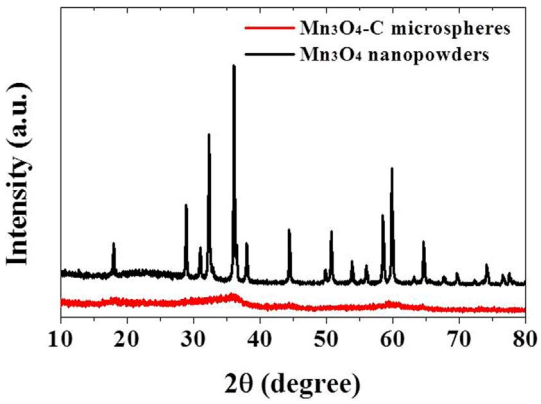

Figure 2 | XRD patterns of the Mn_3O_4-C composite microspheres and Mn_3O_4 nanopowders.

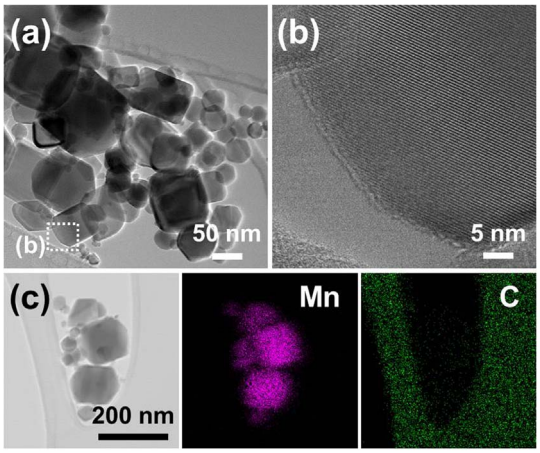

Figure 3 | Morphologies and dot-mapping images of the well-faceted Mn_3O_4 nanopowders prepared by flame spray pyrolysis: (a) TEM image, (b) high-resolution TEM image, and (c) dot-mapping images.

ite microspheres with macropores resembling ant-cave networks. The Mn_3O_4 nanopowders were prepared by one-pot flame spray pyrolysis, similar to the process for preparation of the Mn_3O_4-C composite microspheres. In the flame spray pyrolysis method, a diffusion flame of high temperature above 2500°C was applied to vaporize the manganese oxide powders. The micron-sized manganese oxide powders formed by the drying and decomposition processes of manganese salt solution in the front part of the diffusion flame were completely evaporated into vapors with manganese component. The nucleation and crystal growth process occurring in the rear part of the high temperature diffusion flame produced the Mn_3O_4 nanopowders. The morphologies of the Mn_3O_4 nanopowders prepared by flame spray pyrolysis are shown in Figure 3. The powders as shown in the TEM images have a well-faceted crystal structure possessing various polymorphs. The high resolution TEM image as shown in Figure 3b reveals the single crystalline structure of the Mn_3O_4 nanopowders. The XRD patterns as shown in Figure 2 exhibit the high crystallinity of the Mn_3O_4 nanopowders compared with that of the Mn_3O_4-C composite microspheres. The mean size of the Mn_3O_4 nanopowders measured from the TEM images was 42 nm. The dot-mapping images as shown in Figure 3c reveal the carbon-free of the Mn_3O_4 nanopowders prepared by flame spray pyrolysis.

The electrochemical properties of the Mn_3O_4-C composite microspheres and Mn_3O_4 nanopowders are shown in Figures 4–6. Figures 4a and 4b show the charge and discharge curves for the 1st, 2nd, and 100th cycles of the two samples at a current density of 500 mA g^{-1}. In the voltage range above 0.25 V, inclination in the initial discharge curves of both the Mn_3O_4-C composite microspheres and Mn_3O_4 nanopowders is observed as a result of the irreversible formation of solid-electrolyte interface (SEI) and the initial lithiation process of Mn_3O_4[35,37]. The SEI layer was formed at the surface of the electrode materials during the first discharge process because of irreversible electrochemical decomposition of the liquid electrolyte[38]. The $LiMn_3O_4$ was formed by initial lithiation process of Mn_3O_4[39]. The plateaus of the Mn_3O_4-C composite microspheres and Mn_3O_4 nanopowders at around 0.26 and 0.22 V, respectively, can be attributed to the reduction of Mn_3O_4 to metallic Mn according to the reaction: $Mn_3O_4 + 8\ Li^+ + 8\ e^- \rightarrow 4\ Li_2O + 3\ Mn$[35,37]. The final inclination from the end of plateaus at around 0.2 V to 0.001 V can be attributed to the interfacial lithium insertion[40]. Because of their amorphous-like structure, the Mn_3O_4-C composite microspheres exhibited smaller plateaus in the initial charge and discharge curves compared with those of the Mn_3O_4 nanopowders[41]. The different lithium insertion and extraction characteristics of the Mn_3O_4-C composite microspheres and Mn_3O_4 nanopowders were also shown in the CV curves in Figures 4c and 4d. The Mn_3O_4-C composite microspheres had strong reduction peaks at 0.17 V for the first cycle and at 0.30 V for subsequent cycles. On the other hand, the Mn_3O_4 nanopowders had reduction peaks at 0.03 V for the first cycle and at 0.40 V for subsequent cycles. The main reduction peaks shifted to higher potentials from the second cycle due to the improved kinetics of electrode by formation of ultrafine nanoclusters after the first cycle[42,43]. The oxidation peaks of the Mn_3O_4-C composite microspheres and Mn_3O_4 nanopowders were also different, being exhibited at 1.08 and 1.25 V, respectively. The gradual destruction of the structure of the Mn_3O_4-C composite microspheres during first few cycles decreased the intensities of the CV curves in Figure 4c. Figure 5a shows the cycling performances of the Mn_3O_4-C composite microspheres and Mn_3O_4 nanopowders at a current density of 500 mA g^{-1}. The two samples had similar initial discharge and charge capacities at a high current density of 500 mA g^{-1} because of the short lithium-ion diffusion distances of the two samples. However, the two samples had different cycling properties at a current density of 500 mA g^{-1} as shown in Figure 5a. The discharge capacities of the Mn_3O_4 nanopowders decreased continuously from 1195 to 219 mA h g^{-1} during 100 cycles. On the other hand, the discharge capacities of the Mn_3O_4-C composite microspheres decreased to 452 mA h g^{-1} during the first 26 cycles and then increased to 622 mA h g^{-1} up to 700 cycles. The gradual increase in the capacity of the Mn_3O_4-C composite microspheres was attributed to the formation of a polymeric gel-like film on the active material[44–46]. The gradual destruction of the structure of the Mn_3O_4 nanopowders during cycling decreased the discharge capacities. On the contrary, the structural stability of the Mn_3O_4-C composite microspheres at a high current density resulted in the high discharge capacity of 622 mA h g^{-1} after 700 cycles. The higher Coulombic efficiencies of the Mn_3O_4-C composite microspheres compared with those of the Mn_3O_4 nanopowders during cycling as shown in Figure 5b reveal the structural stability of the composite microspheres. The decrease in discharge capacity during the early stages of the cycling process for the Mn_3O_4-C composite microspheres can be attributed to phase transformation of the crystalline Mn_3O_4 structure to an amorphous-like structure upon cycling[36]. SEM images as exhibited in Figures 5c and 5d revealed the morphologies of the Mn_3O_4-C composite microspheres after 200 and 700 cycles. The images show that the morphology of the Mn_3O_4-C composite microspheres was well maintained even after 700 cycles. The synergistic effects of the macropores and carbon matrix of Mn_3O_4-C composite microspheres resulted in their effective accommodation of volume change and good structural stabilities during cycling. The synergistic effects of the macropores and carbon matrix of Mn_3O_4-C

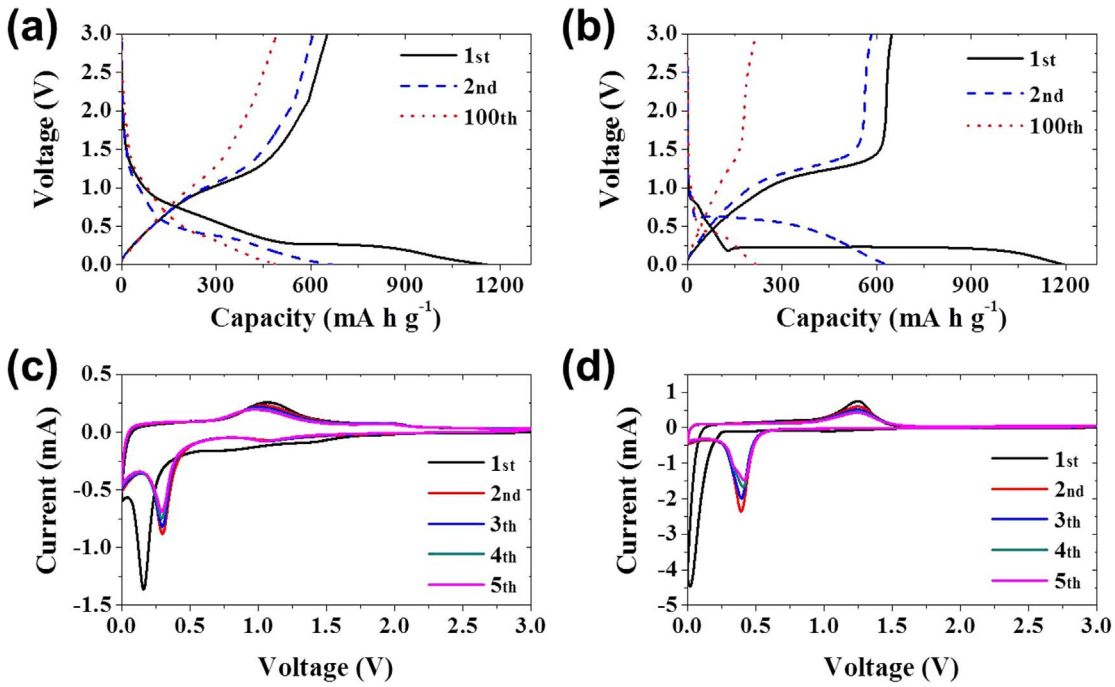

Figure 4 | **Electrochemical properties of the Mn_3O_4-C composite microspheres and Mn_3O_4 nanopowders: (a) and (b) charge/discharge curves of the Mn_3O_4-C composite microspheres and Mn_3O_4 nanopowders at a constant current density of 500 mA g^{-1}, respectively, and (c) and (d) CVs of the Mn_3O_4-C composite microspheres and Mn_3O_4 nanopowders, respecitvely.**

composite microspheres resulted in their effective accommodation of volume change and good structural stabilities during cycling.

Figure 6a shows the rate performances of the Mn_3O_4-C composite microspheres investigated at various current densities between 100 and 900 mA g^{-1}. The composite microspheres had stable discharge capacities after 10 cycles. Therefore, the rate performances of the composite microspheres at current densities between 300 and 900 mA g^{-1} can be estimated from the result of Figure 6a. The discharge capacities of the Mn_3O_4-C composite microspheres at the 10th cycle with consecutive increases in the current densities to 100, 300, 500, 700, and 900 mA g^{-1} were 606, 478, 436, 418, and 401 mA h g^{-1}. The Mn_3O_4-C composite microspheres had good rate performances compared with the Mn_3O_4 nanopowders because of their unique structural properties.

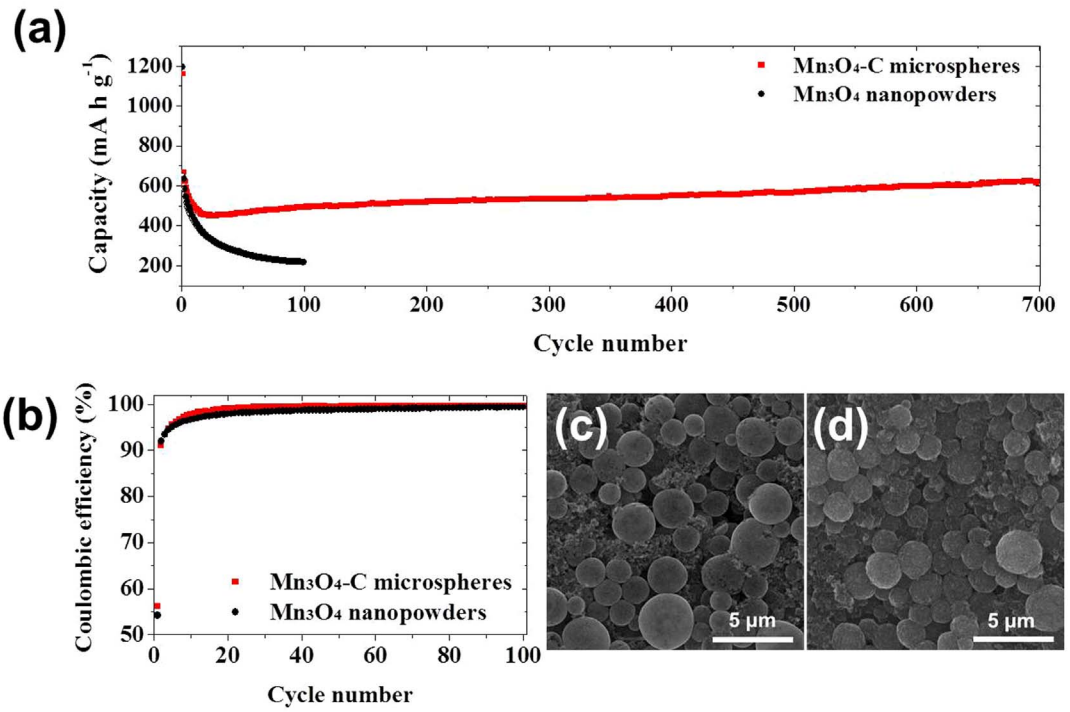

Figure 5 | **(a) Cycling performances and (b) Coulombic efficiencies of the Mn_3O_4-C composite microspheres and Mn_3O_4 nanopowders at a constant current density of 500 mA g^{-1}, and SEM images of the Mn_3O_4-C composite microspheres after (c) 200 and (d) 700 cycles.**

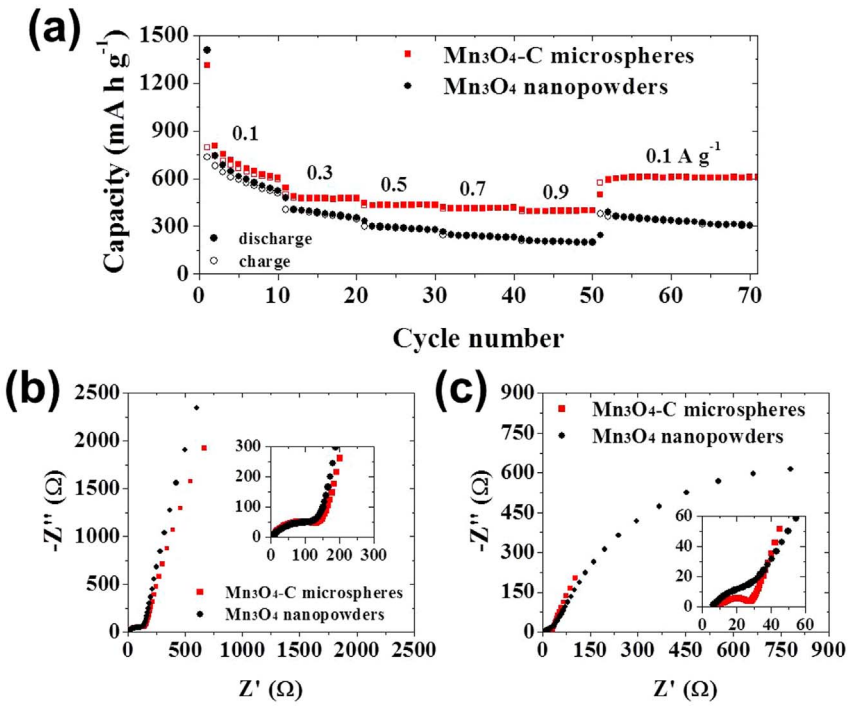

Figure 6 | Electrochemical properties of the Mn_3O_4-C composite microspheres and Mn_3O_4 nanopowders: (a) rate performances and Nyquist plots of the electrochemical impedance spectra (b) before and (c) after 50 cycles at a current density of 500 mA g^{-1}.

Figures 6b and 6c show the impedance spectra of the Mn_3O_4 nanopowders and Mn_3O_4-C composite microspheres with macropores resembling ant-cave networks before and after 50 cycles. The Nyquist plots indicate compressed semicircles in the medium frequency range of each spectrum, which describe the charge transfer resistance (R_{ct}) for these electrodes, and straight lines in the low frequency range, which is associated with Li-ion diffusion in the bulk of the active materials[47,48]. After cycling, both the Mn_3O_4-C composite microspheres and Mn_3O_4 nanopowders present decreased charge transfer resistances because of their phase transformation from crystalline to amorphous during Li-ion insertion/extraction. It is well known that the amorphous-like metal oxides exhibit faster kinetics than crystalline metal oxides. Contrary to the Mn_3O_4 nanopowders, the inclined line in the low frequency range of the Mn_3O_4-C composite microspheres still maintained as shown in Figure 6c. This behavior was contributed to the stable Li-ion diffusion of the Mn_3O_4-C composite microspheres. The Mn_3O_4-C composite microspheres have smaller charge transfer resistance and higher lithium diffusivity after 50 cycles than those of the Mn_3O_4 nanopowders as shown in Figure 6c. Therefore, the Mn_3O_4-C composite microspheres with structural advantages and high electrical conductivity have higher initial discharge and charge capacities and better cycling and rate performances compared to those of the Mn_3O_4 nanopowders.

Discussion

The superior electrochemical performances of the Mn_3O_4-C composite microspheres were attributed to their unique structural features as shown in schematic illustration (Figure S2): (1) The microspheres fabricated by spray pyrolysis comprise a composite of Mn_3O_4 and carbon, with the Mn_3O_4 nanoparticles embedded in amorphous carbon matrix. The amorphous carbon matrix not only accommodates the volume changes during Li-ion insertion/extraction processes but also improves electrical conductivity. (2) The connective and open channels in Mn_3O_4-C composite microspheres can facilitate the electrolyte penetration and reduce the Li-ion pathway. The synergistic effect of these features leads to enhancement of electrochemical performances at high current density and structural stability during cycling.

The Mn_3O_4-C composite microspheres with macropores resembling ant-cave networks and Mn_3O_4 nanopowders were prepared by one-pot spray pyrolysis and flame spray pyrolysis, respectively. One Mn_3O_4-C composite powder was directly formed from one droplet containing Mn salt, PS nanobeads, and sucrose used as the carbon source material. The well-faceted Mn_3O_4 nanopowders were directly prepared from the vapors of manganese oxide by nucleation and growth processes. The Mn_3O_4-C composite microspheres had superior electrochemical properties compared with those of the Mn_3O_4 nanopowders. The discharge capacities of the Mn_3O_4-C composite microspheres at a high current density of 500 mA g^{-1} were 1161 and 622 mA h g^{-1} for the 1st and 700th cycles, respectively. The carbon matrix and open nanochannels improved the cycling and rate performances of the Mn_3O_4-C composite microspheres. In the spray pyrolysis, the porosity and carbon content of the Mn_3O_4-C composite microspheres could be easily controlled by changing the amounts of PS nanobeads and sucrose added into the spray solution, respectively. In addition, the mean size of the Mn_3O_4-C composite microspheres could be controlled by changing the concentration of the spray solution. Fabrication of Mn_3O_4-C composite with controlled morphology and size will result in superior electrochemical performances, making it promising anode materials for LIBs.

Methods

Material fabrication. Mn_3O_4-C composite microspheres with macropores and Mn_3O_4 nanopowders were fabricated using the ultrasonic spray pyrolysis process and flame spray pyrolysis process respectively as described in a previous report[49–51]. The schematic diagrams of the ultrasonic spray pyrolysis and flame spray pyrolysis systems are described in Figure S3. To fabricate the Mn_3O_4-C composite microspheres with macropores, an aqueous spray solution was prepared by dissolving 0.2 M manganese acetate and 0.5 M sucrose in distilled water. Sucrose was used as the carbon source. Subsequently, polystyrene nanobeads (PS) were added to the clear solution, in a weight ratio of 1.5 : 1 with respect to Mn_3O_4. The reactor temperature and flow rate of N_2 carrier gas of the ultrasonic spray pyrolysis system were fixed at 800°C and 10 L min^{-1}. To compare the electrochemical properties, Mn_3O_4 nanopowders were fabricated by flame spray pyrolysis. An aqueous spray solution was prepared by dissolving 0.2 M manganese oxide. The flow rates of the fuel,

oxidizer, and carrier gas of the flame spray pyrolysis system were fixed at 5, 40, and 10 L min^{-1}, respectively.

Characterization. The morphologies of the Mn_3O_4 powders were investigated through scanning electron microscopy (SEM, JEOL JSM-6060) and transmission electron microscopy (FE-TEM, JEM-2100F). Thermal gravimetric analysis (TGA, SDT Q600) was performed in air at a heating rate of 10°C min^{-1} to determine the amount of carbon in the powders. The crystal structures of the powders were investigated by X-ray diffractometry (XRD, X'Pert PRO MPD) using Cu Kα radiation (λ = 1.5418 Å) at the Korea Basic Science Institute (Daegu). The surface area of the powders was measured by the Brunauer-Emmett-Teller (BET) method using N_2 as the adsorbate gas.

Electrochemical measurements. The electrochemical properties of the Mn_3O_4 powders were analyzed in a 2032-type coin cell. The anode was prepared from a mixture of the active material, carbon black, and sodium carboxymethyl cellulose (CMC) in a weight ratio of 7 : 2 : 1. Li metal and a microporous polypropylene film were used as the counter electrode and separator, respectively. The electrolyte was 1 M $LiPF_6$ dissolved in a mixture of fluoroethylene carbonate/dimethyl carbonate (FEC/DMC; 1 : 1 v/v The discharge/charge characteristics of the samples were investigated through galvanostatic tests (wbcs 3000 battery cycler) at a voltage window of 0.001–3 V. Cyclic voltammograms were measured at a scan rate of 0.1 mV s^{-1}. Electrochemical impedance spectra were determined using AC electrochemical impedance spectroscopy (EIS) with a ZIVE SP1 over a frequency range of 0.01 Hz–100 kHz and potential amplitude of 10 mV.

1. Poizot, P., Laruelle, S., Grugeon, S., Dupont, L. & Tarascon, J. M. Nano-sized transition-metal oxides as negative-electrode materials for lithium-ion batteries. *Nature* **407**, 496–499 (2000).
2. Reddy, M. V., Subba Rao, G. V. & Chowdari, B. V. R. Metal oxides and oxysalts as anode materials for Li ion batteries. *Chem. Rev.* **113**, 5364–5457 (2013).
3. Poizot, P., Laruelle, S., Grugeon, S., Dupont, L. & Tarascon, J. M. Searching for new anode materials for the Li-ion technology: time to device from the usual path. *J. Power Sources* **97–98**, 235–239 (2001).
4. Reddy, A. L. M., Shaijumon, M. M., Gowda, S. R. & Ajayan, P. M. Coaxial MnO_2/carbon nanotube array electrodes for high-performance lithium batteries. *Nano Lett.* **9**, 1002–1006 (2009).
5. Chen, J. S. & Lou, X. W. SnO_2-based nanomaterials: synthesis and application in lithium-ion batteries. *Small* **9**, 1877–1893 (2013).
6. Zhou, G. *et al*. Graphene-wrapped Fe_3O_4 anode material with improved reversible capacity and cyclic stability for lithium ion batteries. *Chem. Mater.* **22**, 5306–5313 (2010).
7. Yang, S. *et al*. Porous iron oxide ribbons grown on graphene for high-performance lithium storage. *Sci. Rep.* **2**, 427 (2012).
8. Zhu, X., Zhu, Y., Murali, S., Stoller, M. D. & Ruoff, R. S. Nanostructured reduced graphene oxide/Fe_2O_3 composite as a high-performance anode material for lithium ion batteries. *ACS Nano* **5**, 3333–3338 (2011).
9. Ji, L., Lin, Z., Alcoutlabi, M. & Zhang, X. Recent developments in nanostructured anode materials for rechargeable lithium-ion batteries. *Energy Environ. Sci.* **4**, 2682–2699 (2011).
10. Wang, Z., Zhou, L. & Lou, X. W. Metal oxide hollow nanostructures for lithium-ion batteries. *Adv. Mater.* **24**, 1903–1911 (2012).
11. Wu, H. B., Chen, J. S., Hng, H. H. & Lou, X. W. Nanostructured metal oxide-based materials as advanced anodes for lithium-ion batteries. *Nanoscale* **4**, 2526–2542 (2012).
12. Lai, X., Halpert, J. E. & Wang, D. Recent advances in micro-/nano-structured hollow spheres for energy applications: From simple to complex systems. *Energy Environ. Sci.* **5**, 5604–5618 (2012).
13. Zhang, W. M., Wu, X. L., Hu, J. S., Guo, Y. G. & Wan, L. J. Carbon coated Fe_3O_4 nanospindles as a superior anode material for lithium-ion batteries. *Adv. Funct. Mater.* **18**, 3941–3946 (2008).
14. Lee, K. T., Jung, Y. S. & Oh, S. M. Synthesis of tin-encapsulated spherical hollow carbon for anode material in lithium secondary batteries. *J. Am. Chem. Soc.* **125**, 5652–5653 (2003).
15. Yang, S., Feng, X., Ivanovici, S. & Müllen, K. Fabrication of graphene-encapsulated oxide nanoparticles: towards high-performance anode materials for lithium storage. *Angew. Chem. Int. Ed.* **49**, 8408–8411 (2010).
16. Lou, X. W., Chen, J. S., Chen, P. & Archer, L. A. One-pot synthesis of carbon-coated SnO_2 nanocolloids with improved reversible lithium storage properties. *Chem. Mater.* **21**, 2868–2874 (2009).
17. Lin, J. *et al*. Graphene nanoribbon and nanostructured SnO_2 composite anodes for lithium ion batteries. *ACS Nano* **7**, 6001–6006 (2013).
18. He, C. *et al*. Carbon-encapsulated Fe_3O_4 nanoparticles as a high-rate lithium ion battery anode material. *ACS Nano* **7**, 4459–4469 (2013).
19. Piao, Y., Kim, H. S., Sung, Y. E. & Hyeon, T. Facile scalable synthesis of magnetite nanocrystals embedded in carbon matrix as superior anode materials for lithium-ion batteries. *Chem. Commun.* **46**, 118–120 (2010).
20. Sun, Y., Hu, X., Luo, W. & Huang, Y. Ultrafine MoO_2 nanoparticles embedded in a carbon matrix as a high-capacity and long-life anode for lithium-ion batteries. *J. Mater. Chem.* **22**, 425–431 (2012).
21. Guo, J., Liu, Q., Wang, C. & Zachariah, M. R. Interdispersed amorphous MnO_x-carbon nanocomposites with superior electrochemical performance as lithium-storage material. *Adv. Funct. Mater.* **22**, 803–811 (2012).
22. Lei, C., Han, F., Sun, Q., Li, W. C. & Lu, A. H. Confined nanospace pyrolysis for the fabrication of coaxial Fe_3O_4@C hollow particles with a penetrated mesochannel as a superior anode for Li-ion batteries. *Chem. Eur. J.* **20**, 139–145 (2014).
23. Vu, A., Qian, Y. & Stein, A. Porous electrode materials for lithium-ion batteries - how to prepare them and what makes them special. *Adv. Energy Mater.* **2**, 1056–1085 (2012).
24. Hua, L. & Chen, Q. Hollow/porous nanostructures derived from nanoscale metal–organic frameworks towards high performance anodes for lithium-ion batteries. *Nanoscale* **6**, 1236–1257 (2014).
25. Wang, Y., Zeng, H. C. & Lee, J. Y. Highly reversible lithium storage in porous SnO_2 nanotubes with coaxially grown carbon nanotube overlayers. *Adv. Mater.* **18**, 645–649 (2006).
26. Zhang, H., Yu, X. & Braun, P. V. Three-dimensional bicontinuous ultrafast-charge and -discharge bulk battery electrodes. *Nat. Nanotechnol.* **6**, 277–281 (2011).
27. Lytle, J. C., Yan, H., Ergang, N. S., Smyrl, W. H. & Stein, A. Structural and electrochemical properties of three-dimensionally ordered macroporous tin(iv) oxide films. *J. Mater. Chem.* **14**, 1616–1622 (2004).
28. Wang, Z., Fierke, M. A. & Stein, A. Porous carbon/tin (IV) oxide monoliths as anodes for lithium-ion batteries. *J. Electrochem. Soc.* **155**, A658–A663 (2008).
29. Huang, X. *et al*. Carbon inverse opal entrapped with electrode active nanoparticles as high-performance anode for lithium-ion batteries. *Sci. Rep.* **3**, 2317 (2013).
30. Ko, Y. N., Park, S. B., Jung, K. Y. & Kang, Y. C. One-pot facile synthesis of ant-cave-structured metal oxide-carbon microballs by continuous process for use as anode materials in Li-ion batteries. *Nano Lett.* **13**, 5462–5466 (2013).
31. Li, X. *et al*. Interconnected porous MnO nanoflakes for high-performance lithium ion battery anodes. *J. Mater. Chem.* **22**, 9189–9194 (2012).
32. Wang, T., Peng, Z., Wang, Y., Tang, J. & Zheng, G. MnO nanoparticle@ mesoporous carbon composites grown on conducting substrates featuring high-performance lithium-ion battery, supercapacitor and sensor. *Sci. Rep.* **3**, 2693 (2013).
33. Li, L., Raji, A. R. O. & Tour, J. M. Graphene-wrapped MnO_2–graphene nanoribbons as anode materials for high-performance lithium ion batteries. *Adv. Mater.* **25**, 6298–6302 (2013).
34. Deng, Y. *et al*. Porous Mn_2O_3 microsphere as a superior anode material for lithium ion batteries. *RSC Adv.* **2**, 4645–4647 (2012).
35. Wang, H. *et al*. Mn_3O_4-graphene hybrid as a high-capacity anode material for lithium ion batteries. *J. Am. Chem. Soc.* **132**, 13978–13980 (2010).
36. Li, Z. *et al*. Three-dimensional nanohybrids of Mn_3O_4/ordered mesoporous carbons for high performance anode materials for lithium-ion batteries. *J. Mater. Chem.* **22**, 16640–16648 (2012).
37. Li, L., Guo, Z., Du, A. & Liu, H. Rapid microwave-assisted synthesis of Mn_3O_4–graphene nanocomposite and its lithium storage properties. *J. Mater. Chem.* **22**, 3600–3605 (2012).
38. Pinsona, M. B. & Bazant, M. Z. Theory of SEI formation in rechargeable batteries: capacity fade, accelerated aging and lifetime prediction. *J. Electrochem. Soc.* **160**, A243–A250 (2013).
39. Lowe, M. A., Gao, J. & Abruña, H. D. In operando X-ray studies of the conversion reaction in Mn_3O_4 lithium battery anodes. *J. Mater. Chem. A* **1**, 2094–2103 (2013).
40. Hu, Y. Y. *et al*. Origin of additional capacities in metal oxide lithium-ion battery electrodes. *Nat. Mater.* **12**, 1130–1136 (2013).
41. Ko, Y. N., Choi, S. H., Kang, Y. C. & Park, S. B. Electrochemical properties of ZrO_2-doped V_2O_5 amorphous powders with spherical shape and fine size. *ACS Appl. Mater. Interfaces* **5**, 3234–3240 (2013).
42. Sun, B., Chen, Z., Kim, H. S., Ahn, H. & Wang, G. MnO/C core-shell nanorods as high capacity anode materials for lithium-ion batteries. *J. Power Sources* **196**, 3346–3349 (2011).
43. Sun, Y., Hu, X., Luo, W., Xia, F. & Huang, Y. Reconstruction of conformal nanoscale MnO on graphene as a high-capacity and long-life anode material for lithium ion batteries. *Adv. Funct. Mater.* **23**, 2436–2444 (2013).
44. Grugeon, S., Laruelle, S., Dupont, L. & Tarascon, J. M. An update on the reactivity of nanoparticles Co-based compounds towards Li. *Solid State Ion.* **5**, 895–904 (2003).
45. Zhou, G. *et al*. Graphene-wrapped Fe_3O_4 anode material with improved reversible capacity and cyclic stability for lithium ion batteries. *Chem. Mater.* **22**, 5306–5313 (2010).
46. Courtel, F. M., Duncan, H., Abu-Lebdeh, Y. & Davidson, I. J. High capacity anode materials for Li-ion batteries based on spinel metal oxides AMn_2O_4 (A = Co, Ni, and Zn). *J. Mater. Chem.* **21**, 10206–10218 (2011).
47. Park, M. S., Kang, Y. M., Wang, G. X., Dou, S. X. & Liu, H. K. The effect of morphological modification on the electrochemical properties of SnO_2 nanomaterials. *Adv. Funct. Mater.* **18**, 455–461 (2008).
48. Chen, X., Zhang, N. & Sun, K. Facile fabrication of CuO mesoporous nanosheet cluster array electrodes with super lithium-storage properties. *J. Mater. Chem.* **22**, 13637–13642 (2012).
49. Choi, S. H. & Kang, Y. C. Yolk–shell, hollow, and single-crystalline $ZnCo_2O_4$ powders: preparation using a simple one-pot process and application in lithium-ion batteries. *ChemSusChem* **6**, 2111–2116 (2013).

50. Choi, S. H. & Kang, Y. C. One-pot facile synthesis of Janus-structured SnO_2–CuO composite nanorods and their application as anode materials in Li-ion batteries. *Nanoscale* **5**, 4662–4668 (2013).
51. Ko, Y. N., Kang, Y. C. & Park, S. B. Continuous one-pot synthesis of sandwich structured core–shell particles and transformation to yolk–shell particles. *Chem. Commun.* **49**, 3884–3886 (2013).

Acknowledgments

This work was supported by the National Research Foundation of Korea (NRF) grant funded by the Korea government (MEST) (No. 2012R1A2A2A02046367). This work was supported by the Energy Efficiency & Resources Core Technology Program of the Korea Institute of Energy Technology Evaluation and Planning (KETEP), granted financial resource from the Ministry of Trade, Industry & Energy, Republic of Korea (201320200000420).

Author contributions

Y.N.K. and Y.C.K. devised the concept, designed the experiment, and wrote the manuscript. Y.N.K. and S.H.C. performed the experiments and analyzed the data. S.B.P. analyzed the data and commented on the manuscript. Y.C.K. supervised the project. All authors discussed the results and contributed in this manuscript.

Additional information

Supplementary information accompanies this paper at http://www.nature.com/scientificreports

Competing financial interests: The authors declare no competing financial interests.

How to cite this article: Ko, Y.N., Park, S.B., Choi, S.H. & Kang, Y.C. One-pot synthesis of manganese oxide-carbon composite microspheres with three dimensional channels for Li-ion batteries. *Sci. Rep.* **4**, 5751; DOI:10.1038/srep05751 (2014).